Estimation of all-sky instantaneous surface incident shortwave radiation from Moderate Resolution Imaging Spectroradiometer data using optimization method

Yi Zhang[1], Tao He[2], Shunlin Liang[1,*], Dongdong Wang[1] and Yunyue Yu[3]

1, Department of Geographical Science, University of Maryland, College Park, MD, 20742, USA
2, School of Remote Sensing and Information Engineering, Wuhan University, Wuhan, China, 430079
3, NOAA/NESDIS/Center for Satellite Applications and Research, College Park, MD, USA, 20740
*, Corresponding author, sliang@umd.edu

Abstract

Surface incident shortwave radiation (ISR) is a crucial parameter in the land surface radiation budget. Many reanalysis, observation-based, and satellite-derived global radiation products have been developed but often have insufficient accuracy and spatial resolution for many applications. In this paper, we propose a method based on a radiative transfer model for estimating surface ISR from Moderate Resolution Imaging Spectroradiometer (MODIS) Top of Atmosphere (TOA) observations by optimizing the surface and atmospheric variables with a cost function. This approach consisted of two steps: retrieving surface bidirectional reflectance distribution function parameters, aerosol optical depth (AOD), and cloud optical depth (COD); and subsequently calculating surface ISR. Validation against measurements at seven Surface Radiation Budget Network (SURFRAD) sites resulted in an R^2 of 0.91, a bias of -6.47 W/m^2, and a root mean square error (RMSE) of 84.17 W/m^2 (15.12%) for the instantaneous results. Validation at eight high-latitude snow-covered Greenland Climate Network (GC-Net) sites resulted in an R^2 of 0.86, a bias of -21.40 W/m^2, and an RMSE of 84.77 W/m^2 (20.96%). These validation results show that the proposed method is much more accurate than the previous studies (usually with RMSEs of 80-150W/m^2). We further investigated whether incorporating additional satellite products, such as the MODIS surface broadband albedo (MCD43), aerosol

(MOD/MYD04), and cloud products (MOD/MYD06), as constraints in the cost function would improve the accuracy. When the AOD and COD estimates were constrained, RMSEs were reduced to 62.19 W/m^2 (12.12%) and 71.70 W/m^2 (17.74%) at the SURFRAD and GC-Net sites, respectively. This algorithm could estimate surface ISR with MODIS TOA observations over both snow-free and seasonal/permanent snow-covered surfaces. The algorithm performed well at high-latitude sites, which is very useful for radiation budget research in the polar regions.

Keywords: Incident shortwave radiation, Optimization, Aerosol optical depth, Cloud optical depth

1. **Introduction**

Surface incident shortwave radiation (ISR) is the irradiance that reaches the Earth's surface in the shortwave spectral range, usually between 300 and 3000 nm. As the main energy source for the Earth's surface, ISR drives energetic, hydrological, and ecological dynamics at the Earth's surface and controls the energy and water exchanges between the surface and atmosphere (Liang et al. 2010). Efforts have been made in the estimation of ISR for several decades. Currently, many global and regional networks provide ISR measurements, such as the Surface Radiation Budget Network (SURFRAD) (Augustine et al. 2000), FLUXNET (Baldocchi et al. 2001), Baseline Surface Radiation Network (Ohmura et al. 1998), Global Energy Balance Archive (Gilgen and Ohmura 1999; Wild et al. 2013), Greenland Climate Network (GC-NET) (Steffen et al. 1996), and Atmospheric Radiation Measurement. In-situ measurements are believed to have higher accuracy than other sources but have limited spatial coverage and representativeness. For better spatial coverage, many reanalysis and satellite-derived ISR products have been published, which are often validated with in-situ measurements. However, existing reanalysis and satellite-derived products are usually limited by accuracy and spatial resolution for many applications. The World Meteorological Organization Observing System Capability Analysis and Review Tool proposed requirements for ISR: “Goal,” “Breakthrough,” and “Threshold” are three levels of requirements, ranging from “ultimate” to “acceptable” targets. Many researchers have evaluated widely used reanalysis and satellite-derived ISR products. Zhang et al. (2015; 2016) showed the insufficient spatial resolution and accuracy among existing products. All the widely used ISR products’ spatial resolutions are coarser than 0.3°, which fails to meet the 20 km basic “threshold” requirement for agricultural meteorology. Moreover, the best performance in terms of root mean square error (RMSE) among these products is Clouds and Earth’s Radiant Energy System Energy Balanced and Filled (CERES-EBAF), which has a monthly RMSE of 18.8 W/m^2 and still fails to meet the basic “threshold” requirement for all applications in terms of either temporal resolution (daily) or uncertainty.

The published algorithms for estimating ISR from satellite data can be categorized into three groups: parameterization, look-up table (LUT), and machine learning methods. Most parameterization methods use satellite-derived atmospheric products to calculate ISR from parameterized equations (Bisht and Bras 2010; Forman and Margulis 2009; Qin et al. 2015; Tang et al. 2016; Van Laake and Sanchez-Azofeifa 2004). Different components of atmospheric effects (such as aerosol absorption/scattering, cloud reflection, and gas absorption) are usually parameterized separately according to their physical bases. The general idea of LUT methods is a simplification of radiative transfer simulation (Huang et al. 2016b; Huang et al. 2011; Liang et al. 2006; Zhang et al. 2014): ISR can be simulated by radiative transfer models with the input of atmospheric and surface parameters (e.g., aerosol, cloud, water vapor, and surface albedo), but due to the limited efficiency of the radiative transfer calculation, only selected cases of combinations ("bins") are calculated and stored in an offline LUT. When the ISR is estimated online, the simulation results are interpolated according to the value of the parameters. Machine learning methods link ISR and satellite images with statistical relationships (Aguiar et al. 2015; Akarslan and Hocaoglu 2016; Akarslan et al. 2014; Janjai et al. 2009; Mefti et al. 2008; Tang et al. 2016).

However, all three types of algorithms have corresponding limitations. Parameterization, LUT and some of the machine learning algorithms require atmospheric products as input, but some atmospheric products, such as aerosol optical depth (AOD), are hard to estimate (Levy et al. 2010) and bring uncertainties into the estimation of ISR. LUT algorithms usually use linear interpolation to calculate parameters within the pre-calculated bins, which sometimes brings uncertainties. LUT methods further have to balance efficiency and accuracy. Thus, the dimensions and bins of the LUT have to be limited. Machine learning algorithms essentially rely on a statistical relationship to estimate ISR and lack a physical basis. The performances highly depend on the quantity and representativeness of the training data.

In this paper, we present an optimization-based method to estimate ISR from Moderate Resolution Imaging Spectroradiometer (MODIS) TOA spectral reflectance. This algorithm can estimate ISR using only MODIS TOA reflectance, and multiple products are optional input for the algorithm as constraints. Our algorithm optimizes both atmospheric and surface parameters simultaneously with a radiative transfer model and a cost function, from which ISR is estimated with a pre-calculated LUT. Validation against ground measurements at seven SURFRAD sites and 8 GC-Net sites in 2013 was conducted to evaluate the algorithm's performance in different climate regions with various land cover types. Section 2 of this paper describes the theoretical concepts and includes a brief introduction to the retrieval algorithm. Section 3 describes the datasets used in this study. Validation results are presented and discussed in Section 4, and a summary is presented in Section 5.

2. **Methodology**

2.1 Optimization of surface bidirectional reflectance distribution function parameters and atmospheric optical depth

The method for the optimization of bidirectional reflectance distribution function (BRDF) parameters was originally developed for the estimation of surface reflectance, albedo, and AOD under cloud-free conditions (He et al. 2012). We extended the algorithm for estimating instantaneous ISR from MODIS data. Figure 1 shows the framework of the ISR estimation algorithm.

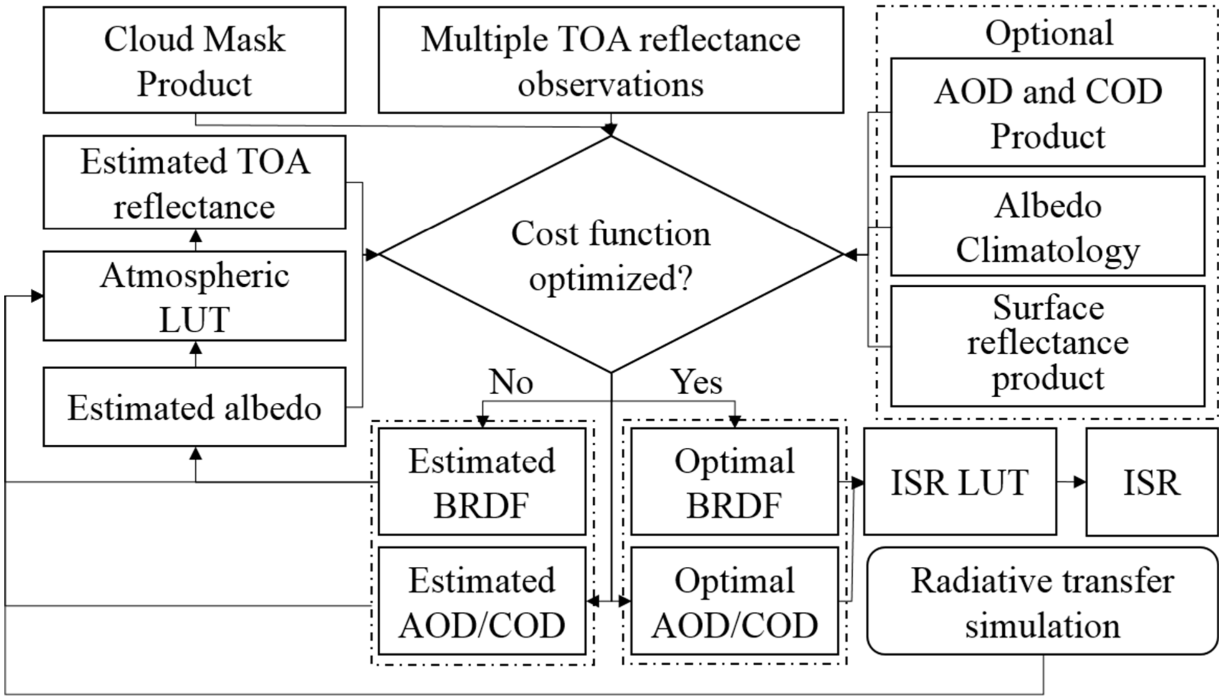

Figure 1 Framework of the ISR estimation algorithm

2.1.1 Calculation of TOA reflectance

The spectral TOA reflectance in the first seven spectral bands was calculated via surface and atmospheric parameters through radiative transfer simulation. The calculated TOA reflectance was used to build a cost function, which was used to determine the optimums of surface and atmospheric parameters.

Many simplified forward models, including various two-stream (Meador and Weaver 1980) and four-stream methods (Liang and Strahler 1994, 1995), have been proposed to approximate radiative parameters. However, these models sacrifice accuracy for higher efficiency. This study adopted the formulation of radiative transfer incorporating the surface BRDF model and separating the radiation field into direct and diffuse components in both upwelling and downward directions. This formulation is accurate although calculating the reflectance and transmittance terms in the formula requires numerical approximations (Qin et al.

2001). The TOA reflectance is as follows:

$$\rho(\Omega_s, \Omega_v) = \rho_0(\Omega_s, \Omega_v) + \frac{T(\Omega_s)R(\Omega_s,\Omega_v)T(\Omega_v) - t_{dd}(\Omega_s)t_{dd}(\Omega_v)|R(\Omega_s,\Omega_v)|}{1 - r_{hh}\rho} \quad (1)$$

$$T(\Omega_s) = [t_{dd}(\Omega_s), t_{dh}(\Omega_s)] \quad (2)$$

$$T(\Omega_v) = [t_{dd}(\Omega_v), t_{hd}(\Omega_v)]^T \quad (3)$$

$$R(\Omega_s, \Omega_v) = \begin{bmatrix} r_{dd}(\Omega_s, \Omega_v) & r_{dh}(\Omega_s) \\ r_{hd}(\Omega_v) & r_{hh} \end{bmatrix} \quad (4)$$

Where Ω_s and Ω_v denote the solid angles of the solar and viewing directions, respectively. $\rho_0(\Omega_s, \Omega_v)$ is the reflectance normalized by path radiance and is controlled only by the atmosphere. $\frac{T(\Omega_s)R(\Omega_s,\Omega_v)T(\Omega_v) - t_{dd}(\Omega_s)t_{dd}(\Omega_v)|R(\Omega_s,\Omega_v)|}{1 - r_{hh}\rho}$ is controlled by the interaction between the surface and atmosphere. In the second term, *T* and *R* denote a transmittance and reflectance matrix (Equations 3 and 4), respectively, while *t* and *r* represent bi-directional transmittance and reflectance, respectively. ρ is the atmospheric spherical albedo, and $T(\Omega_s)$ and $T(\Omega_v)$ are combinations of direct and diffuse transmittance, respectively.

Here, *d* denotes “directional” and *h* denotes “hemisphere.” Thus, $t_{dd}(\Omega_v)$ is direct transmittance and $t_{hd}(\Omega_v)$ is diffuse transmittance. In practice, it is usually time-consuming to calculate all the atmospheric parameters in each pixel online. To make computation more time-efficient the atmospheric parameters were pre-calculated offline by simulation using the radiative transfer software libRadtran (Mayer and Kylling 2005) and stored in the LUT.

In terms of the surface, *d* denotes “directional” and *h* denotes “hemisphere.” r_{hh} and $r_{dh}(\Omega_s)$ represent white and black-sky albedo, respectively. All of the parameters can be calculated with surface BRDF parameters. The surface BRDF model and the atmospheric radiative transfer simulation are presented in Sections 2.1.2 and 2.1.3, respectively.

2.1.2 Surface BRDF model

BRDF models quantify angular distribution parameters of surface-reflected radiance. Various models have been proposed to simulate anisotropic characteristics of the surface. These BRDF models can be divided into three main groups, namely computer simulation, physical, and semi-empirical models. Pokrovsky and Roujean (2003a, b) compared different kernel-based BRDF models and found that the Li–Sparse and Roujean models have the best performance. The improved Ross–Li kernel model by Maignan (2004) and Breon (2002) is used to calculate the surface anisotropic reflectance:

$$R(\Omega_s, \Omega_v, \varphi) = f_{iso} + f_{vol}K_{vol}(\Omega_s, \Omega_v, \varphi) + f_{geo}K_{geo}(\Omega_s, \Omega_v, \varphi) \quad (5)$$

Where, Ω_s, Ω_v, and φ are the solar zenith, view zenith, and relative azimuth angles, respectively. K_{vol} is a kernel based on the approximation of the radiative transfer for canopy, and K_{geo} is a kernel based on the distribution of the surface canopy size and orientation. f_{iso}, f_{vol}, and f_{geo} are the coefficients for these kernels.

2.1.3 Atmospheric radiative transfer simulation

Atmospheric optical parameters such as spherical albedo, atmospheric downward/upward transmittance, and path reflectance are required to implement a forward simulation using Equation 3. To make the algorithm more efficient, all of the parameters were pre-calculated in representative geometries and atmospheric conditions (AOD and cloud optical depth [COD]). Again, libRadtran (Mayer and Kylling 2005) software was used for the generation of the LUT. The following values were used as entries in the radiative transfer simulations: solar zenith angle (0°–80°, at 5° intervals), viewing zenith angle (0°–80°, at 5° intervals), relative azimuth angle (0°–180°, at 10° intervals), COD (1, 2, 3, 5, 10, 20, 30, 40, 50, 60, 70, 80, 90, 100), AOD at 550 nm (0.01, 0.025, 0.05, 0.1, 0.2, 0.3, 0.4, 0.5, 0.6, 0.7, 0.8, 0.9, 1.0), and water vapor (0, 15, 30, 45, 60, 75, 90, 105 mm).

We used the continental-clean model to estimate ISR at the SURFRAD sites and the Antarctic model to estimate ISR at the GC-Net sites. For each specific solar/viewing geometry and atmospheric parameter (AOD at 550 nm for clear-sky conditions or COD for cloudy-sky conditions), radiative transfer simulations generated path reflectance, upward/downward transmittances, and spherical albedo for each of the seven MODIS bands. We used actual site elevation to estimate ISR at the SURFRAD and GC-NET sites. With the atmospheric LUT, we calculated the surface broadband albedo and atmospheric index (AOD and COD) from the optimization process. ISR could then be calculated under certain geometries using the surface radiation LUT. In this paper, we calculated the ISR for the spectral range of 280–2800 nm to match the field measurements.

2.1.4 Cost function and optimization

The TOA spectral reflectance calculated from the steps described Sections 2.1.1–2.1.3 was used to build up the following cost function:

$$J(X) = (R^{est}(X) - R^{obs}(X))O^{-1}(R^{est}(X) - R^{obs}(X)) + J_c + [(A(X) - A^{clm})B^{-1}(A(X) - A^{clm}) + (C(X) - C^{est})I^{-1}(C(X) - C^{est}) + (D(X) - D^{est})I^{-1}(D(X) - D^{est})] \quad (6)$$

$$X_{clr} = [BRDF_1, BRDF_2, \dots, BRDF_{NB}, AOD_1, AOD_2, \dots, AOD_{NO}]^T \quad (7)$$

$$X_{cld} = [COD_1, COD_2, \dots, COD_{NO}]^T \quad (8)$$

Where *NB* is the number of spectral bands, and *NO* is the number of clear-sky observations. $BRDF_i$ is a set of BRDF kernel parameters. AOD_j and COD_j are the AOD and COD values of corresponding observations, respectively. R^{obs} and R^{est} are satellite-observed TOA reflectance and simulated TOA reflectance from the radiative transfer model for one band and one geometry (solar zenith, viewing zenith, and relative azimuth angles), respectively.

The terms in the square brackets are optional constraints in Equation 6. $A(X)$ is the calculated surface shortwave broadband albedo from the retrieved BRDF parameters, and A^{clm} is the broadband albedo climatology. The albedo climatology is used to constrain the retrieving procedure. It characterizes the major seasonal and annual changes in surface albedo. Multiyear MODIS albedo products were collected to generate the spatially and temporally continuous albedo climatology. $C(X)$ is the calculated AOD at 550 nm, and C^{est} is the MODIS MOD/MYD04 AOD data. $D(X)$ is the calculated COD, and D^{est} is the MODIS MOD/MYD06 COD data. The AOD and COD products were used to constrain the retrieving procedure of atmospheric parameters. Jc denotes the penalty part of the cost function. In any particular geometry, if the reflectance or albedo calculated from the BRDF model is negative or greater than one, *Jc* is set to a large punitive value. In this framework, the AOD and COD can be the by-product of ISR when they are not available as input. However, if AOD and COD were provided as input, they could serve as constraints in the cost function to improve the accuracy.

Here, X denotes unknown parameters within the time window (8 days). In the clear-sky case, X_{clr} included surface BRDF parameters and AOD. An assumption was made that the surface BRDF parameters and aerosol types were stable within the time window. In the cloudy-sky case, surface parameters were usually unavailable, and the BRDF parameters optimized from clear-sky cases were used as input; X_{cld} only included the COD.

In one single time step, the unknown parameters included three BRDF parameters for each spectral band and the atmospheric parameters (AOD/COD), while the information number was equal to the number of bands (NB). An assumption was needed to make the optimization solvable. Usually, the change of surface is much slower than that of the atmosphere, and we therefore assumed that the surface BRDF parameters remained constant within a time window. In this paper, the time window was eight days to obtain enough clear observations. The Shuffled

Complex Evolution algorithm (Duan et al. 1994) was used to search for the optimum.

2.2 Calculation of instantaneous ISR

The ISR was estimated with Equations 9 and 10 (Liang et al. 2006):

$$F(\mu_0) = F_0(\mu_0) + \frac{r_s\bar{\rho}}{1-r_s\bar{\rho}}\mu_0 E_0 \gamma(\mu_0) \quad (9)$$

$$F_0(\mu_0) = F_{dir}(\mu_0) + F_{dif}(\mu_0) \quad (10)$$

Where, $F_0(\mu_0)$ is the radiation without any contribution from the surface, and $F_{dir}(\mu_0)$ and $F_{dif}(\mu_0)$ denote the direct and diffuse parts, respectively. r_s is the surface reflectance, $\bar{\rho}$ is the spherical albedo, μ_0 is the cosine of the solar zenith angle, E_0 is the extraterrestrial solar irradiance, and $\gamma(\mu_0)$ is the total trnasmittance. For each combination of geometry and optical depth, $F_0(\mu_0)$, $\bar{\rho}$, and $\mu_0 E_0 \gamma(\mu_0)$ were pre-calculated by radiative transfer simulation and stored in the LUT. The ISR was the integration of the flux from 280 to 2800 nm. The optimized BRDF parameters and AOD/COD were used to estimate instantaneous ISR according to the LUT.

2.3 Cloud screening

In the validation procedure, we introduced a cloud-screening process. The 3-D structure of clouds may cause different views from the sensor and the site tower. Sometimes the sensor view is cloudy but the tower view is clear, vice versa. The cloud-screening procedure was designed to lower this effect. As shown in Figure 2, the ratio between direct ISR and total ISR was mainly determined by the optical depth. We calculated the "cloud mask" for each SURFRAD observation based on site-observed direct/total ISR ratio and radiative simulation. If the direct ISR ratio from the site observation was less than the simulated ratio at an optical depth of 1, the site observed cloud mask was defined as cloudy, otherwise it was deemed clear. In the cloud-screening process, if the MODIS cloud mask data product differed from the cloud mask of the corresponding SURFRAD observation, the observation was included in the validation. A total of 5.75% of observations was removed in this process. The GC-Net observations provided only total ISR, and therefore the cloud-screening process was only used at the SURFRAD sites.

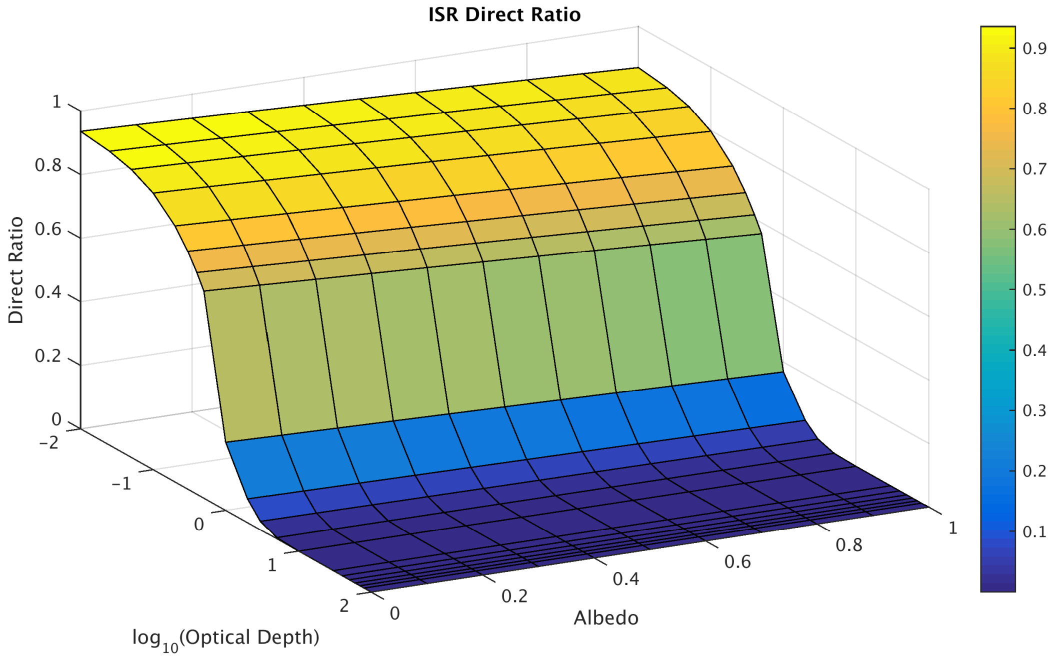

Figure 2 Impact of optical depth and surface albedo on the direct ISR ratio from radiative simulation

3. **Data**

3.1 **MODIS data**

MODIS provided seven spectral bands in the shortwave range (bands 1–7) that can be used in this application. We transformed the MODIS Level 1B C6 calibrated radiance data into TOA bidirectional reflectance. In the clear-sky model, for a given observation number N, the input data were the TOA reflectance observations from the seven spectral bands, and the unknown variables were the three BRDF kernel parameters for each band and the N AOD values.

The BRDF parameters were wavelength-dependent and were unknown for the seven bands of each observation. Because there were fewer observations than unknown variables, an assumption needed to be made to solve the underdetermined problem. We assumed that the surface BRDF kernel parameters were stable and invariant within a sliding time window. To guarantee an invertible process, the number of input parameters had to be no less than the number of unknown variables. Therefore, N had to be at least four.

MODIS level 2 cloud mask products (MOD/MYD35_L2) were used to distinguish clear and cloudy condition observations. MODIS level 2 water vapor products (MOD/MYD05) were used for water vapor correction. In addition, several MODIS products were used as optional constraints in the optimization procedure. The MODIS level 2 aerosol product (MOD/MYD04) provided AOD data, and the cloud product (MOD/MYD06) provided COD data. The AOD and COD data were used as constraints for the atmospheric conditions in the optimization process in the clear-sky and cloudy-sky models, respectively. MODIS surface reflectance data (MOD/MYD09) were used as optional input in the cloudy-sky model. Ten years (2000–2009) of MODIS broadband albedo products and quality control data were collected, and albedo data marked as “good quality” were used to calculate the climatology.

3.2 **Ground measurements**

Ground measurements from seven SURFRAD (Augustine et al. 2000) sites and 8 GC-Net (Steffen et al. 1996) sites in 2013 were used in this study to validate ISR. All the GC-Net sites with available field measurements were included. The GC-Net sites collected shortwave radiation observations every hour, and these data facilitated validation of the algorithm accuracy over the snow-covered surface. We matched the estimation results with the closest ground measurement in the temporal domain within 30 min (Huang et al. 2016a) at the SURFRAD sites.

Table 1 shows the site information of the sites used in this study.

Table 1 SURFRAD and GC-Net sites for validation

Site Name	Latitude	Longitude	Elevation(m)
Fort Peck	48.31	-105.10	634
Sioux Falls	43.73	-96.62	473
Penn State	40.72	-77.93	376
Bondville	40.05	-88.37	230
Boulder	40.13	-105.24	1689
Desert Rock	36.62	-116.02	1007
NASA-U	73.84	-49.51	2334
Humboldt	78.53	-56.83	1995
Summit	72.58	-38.51	3199
Tunu-N	78.02	-33.98	2052
DYE-2	66.48	-46.28	2099
Saddle	66.00	-44.50	2467
NASA-SE	66.48	-42.50	2373
NEEM	77.50	-50.87	2454

We used the quality assurance flag to eliminate uncertainties from the MODIS cloud mask product. The MOD/MYD35 data provided a “confidence level” quality flag. We eliminated data marked as “no confidence” and only used the data with a quality assurance of “intermediate confidence,” “high confidence,” or “very high confidence.”

4. Results and discussion

4.1 Validation with SURFRAD site measurements

Comparisons between retrieved surface ISR and ground measurements for the SURFRAD sites are shown in Figures 3, 4, and 5. The validation results show an R^2 of 0.96, a bias of 7.07 W/m^2, and an RMSE of 62.19 W/m^2 (12.12%) for instantaneous ISR. The RMSEs for clear and cloudy condition validation were 41.85 and 71.75 W/m^2, respectively.

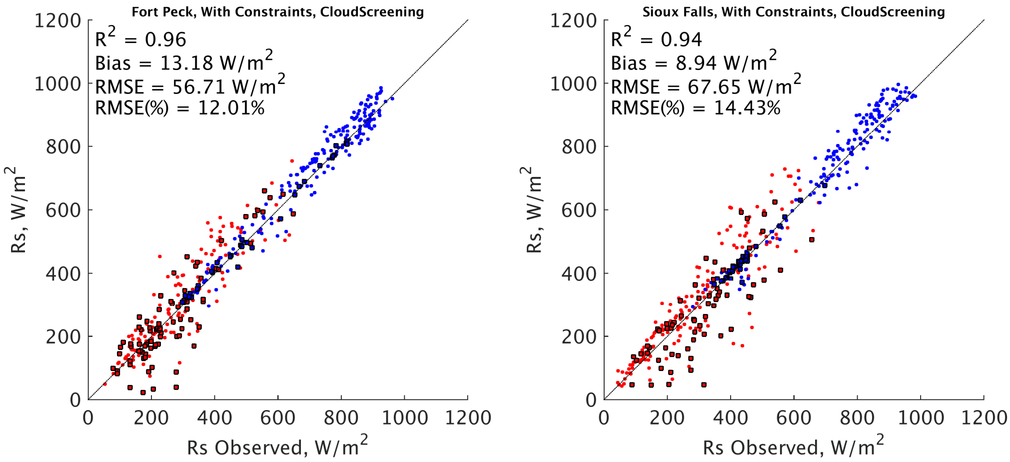

Fort Peck, With Constraints, CloudScreening
R^2 = 0.96
Bias = 13.18 W/m^2
RMSE = 56.71 W/m^2
RMSE(%) = 12.01%
Rs, W/m^2
Rs Observed, W/m^2
Sioux Falls, With Constraints, CloudScreening
R^2 = 0.94
Bias = 8.94 W/m^2
RMSE = 67.65 W/m^2
RMSE(%) = 14.43%
Rs, W/m^2
Rs Observed, W/m^2

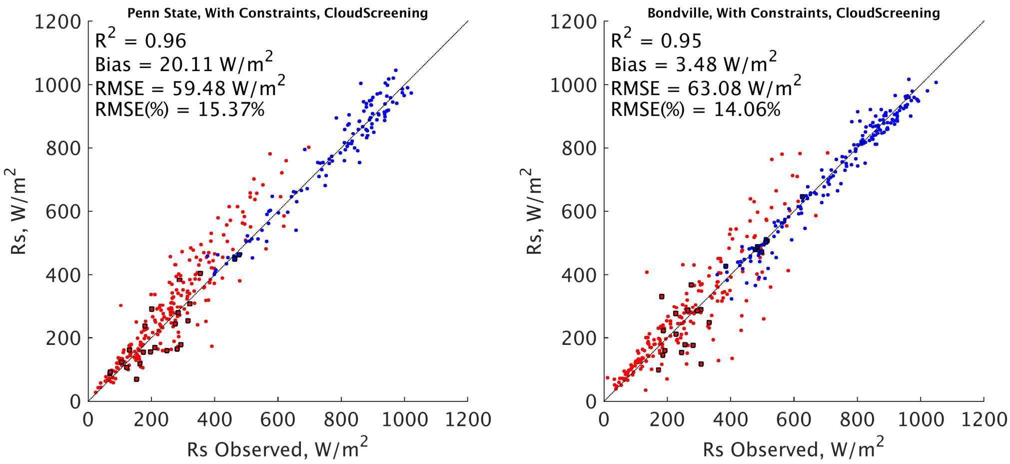

Penn State, With Constraints, CloudScreening
R^2 = 0.96
Bias = 20.11 W/m^2
RMSE = 59.48 W/m^2
RMSE(%) = 15.37%
Rs, W/m^2
Rs Observed, W/m^2
Bondville, With Constraints, CloudScreening
R^2 = 0.95
Bias = 3.48 W/m^2
RMSE = 63.08 W/m^2
RMSE(%) = 14.06%
Rs, W/m^2
Rs Observed, W/m^2

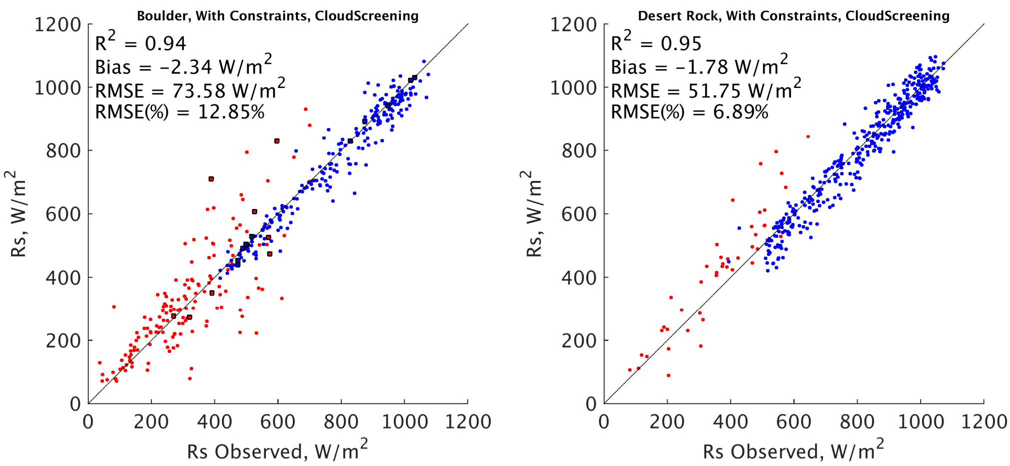

Boulder, With Constraints, CloudScreening
R^2 = 0.94
Bias = -2.34 W/m^2
RMSE = 73.58 W/m^2
RMSE(%) = 12.85%
Rs, W/m^2
Rs Observed, W/m^2
Desert Rock, With Constraints, CloudScreening
R^2 = 0.95
Bias = -1.78 W/m^2
RMSE = 51.75 W/m^2
RMSE(%) = 6.89%
Rs, W/m^2
Rs Observed, W/m^2

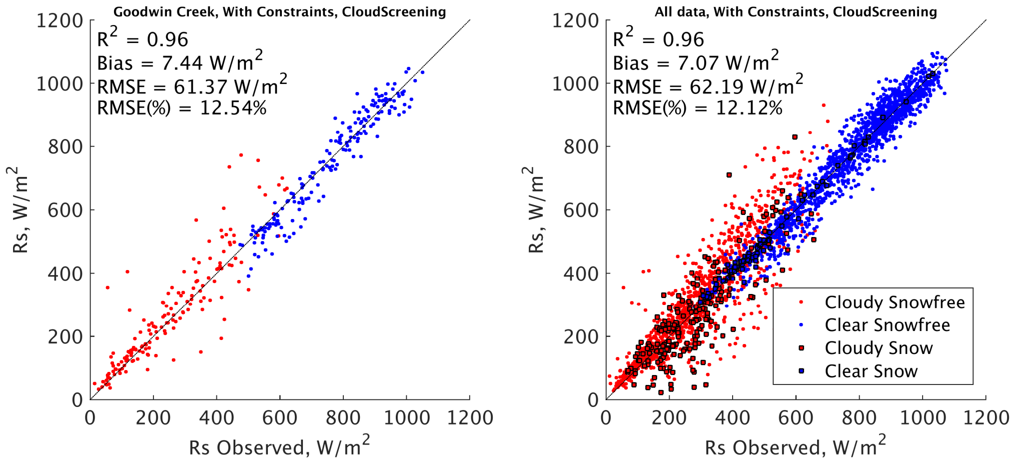

Figure 3 Scatterplot of instantaneous ISR in 2013 at SURFRAD sites. Result calculated with AOD and COD product as constraints. (Blue: clear-sky results, Red: cloudy-sky results, Points: snow-free results, Squares: Snow covered results)

Figure 4 shows a time series of the validation results for each site. The retrieved ISR could sufficiently characterize seasonal change. The Desert Rock site had a higher clear-sky observation ratio than other sites did and thus had the lowest RMSE and bias error.

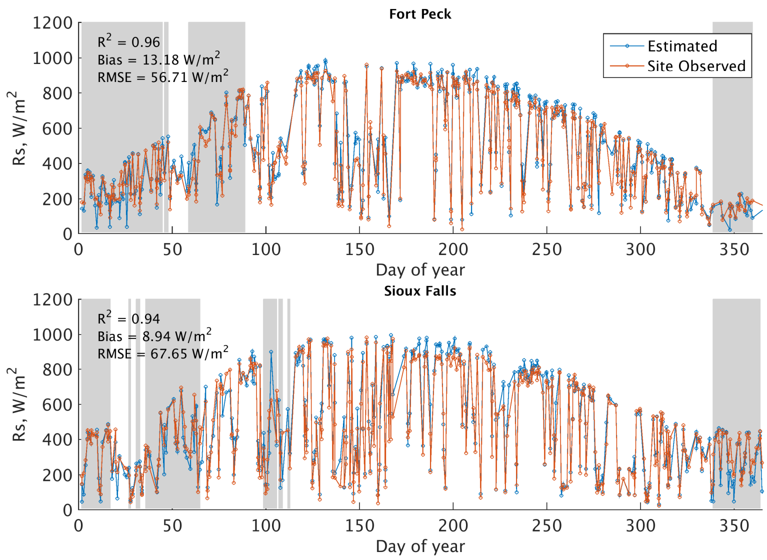

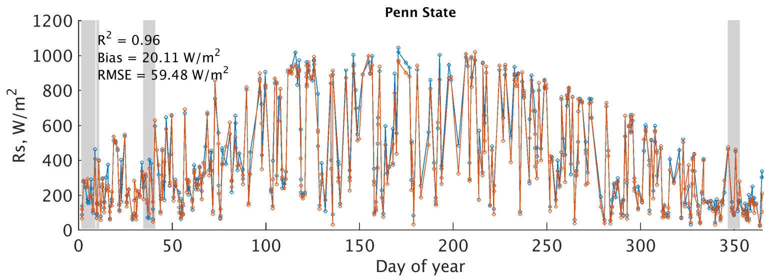
Penn State
R² = 0.96
Bias = 20.11 W/m²
RMSE = 59.48 W/m²
Rs, W/m²
Day of year

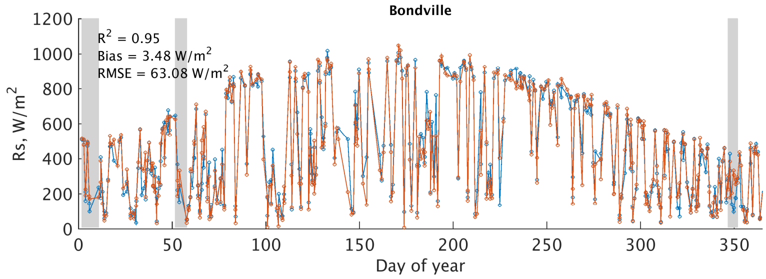
Bondville
R² = 0.95
Bias = 3.48 W/m²
RMSE = 63.08 W/m²
Rs, W/m²
Day of year

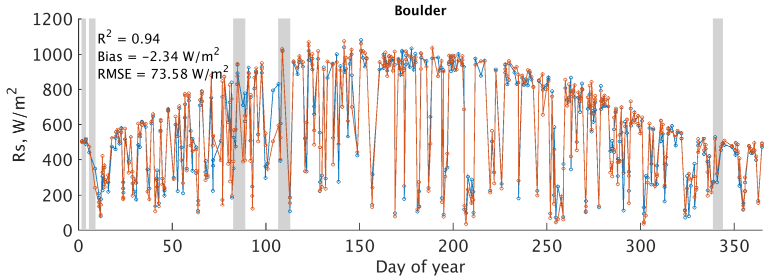
Boulder
R² = 0.94
Bias = -2.34 W/m²
RMSE = 73.58 W/m²
Rs, W/m²
Day of year

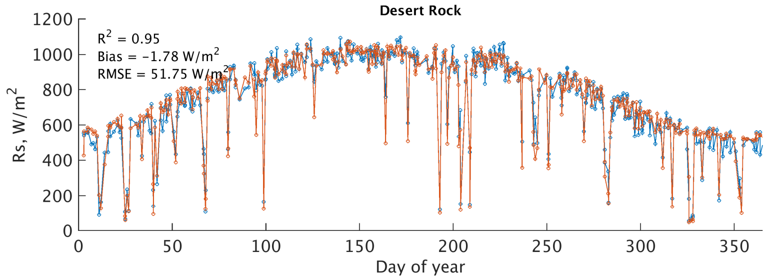
Desert Rock
R² = 0.95
Bias = -1.78 W/m²
RMSE = 51.75 W/m²
Rs, W/m²
Day of year

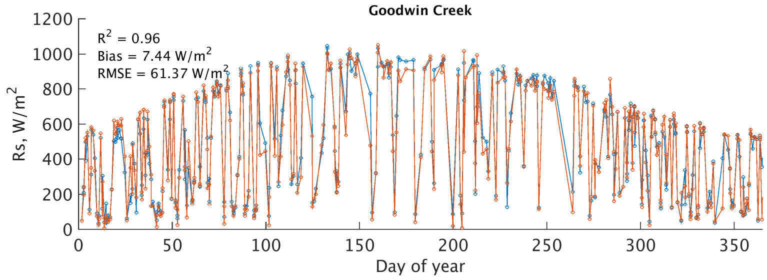
Goodwin Creek
R² = 0.96
Bias = 7.44 W/m²
RMSE = 61.37 W/m²
Rs, W/m²
Day of year

Figure 4 Validation of time series for instantaneous ISR in 2013 at SURFRAD sites. Result calculated with AOD and COD product as constraints. (Blue: estimated results, Red: SURFRAD site observation data, the gray area denotes observation over snow)

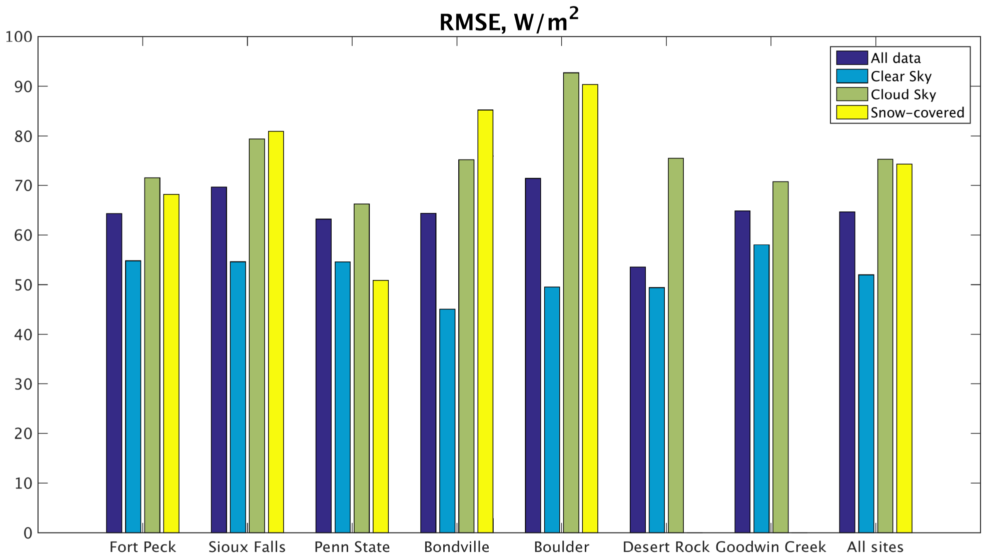

Figure 5 Validation RMSE for clear/cloudy/all sky and over snow at SURFRAD sites

The clear-sky results show similar RMSEs among all sites. The cloudy-sky results show the largest RMSE in the Boulder site. The Boulder site is located in Table Mountain, which is more easily affected by sparse cloud cover. Furthermore, the Boulder site had the largest difference between clear-sky and cloudy-sky results. For clear-sky results, all seven sites had an RMSE of less than 60 W/m^2. The all-sky results for all seven sites had a bias error of less than 15 W/m^2 and an RMSE of less than 75 W/m^2.

4.2 Validation with GC-Net site measurements

Comparisons between retrieved surface ISR and ground measurements for the GC-Net sites are shown in Figures 6, 7, and 8. The validation results show an R^2 of 0.89, a bias of -15.77

W/m², and an RMSE of 71.70 W/m² (17.74%) for instantaneous ISR. The RMSEs for clear-sky and cloudy-sky validations were 56.14 and 86.69 W/m², respectively. The clear- and cloudy-sky observations were masked by the MODIS cloud mask product, which may have more uncertainties over Arctic areas due to snow.

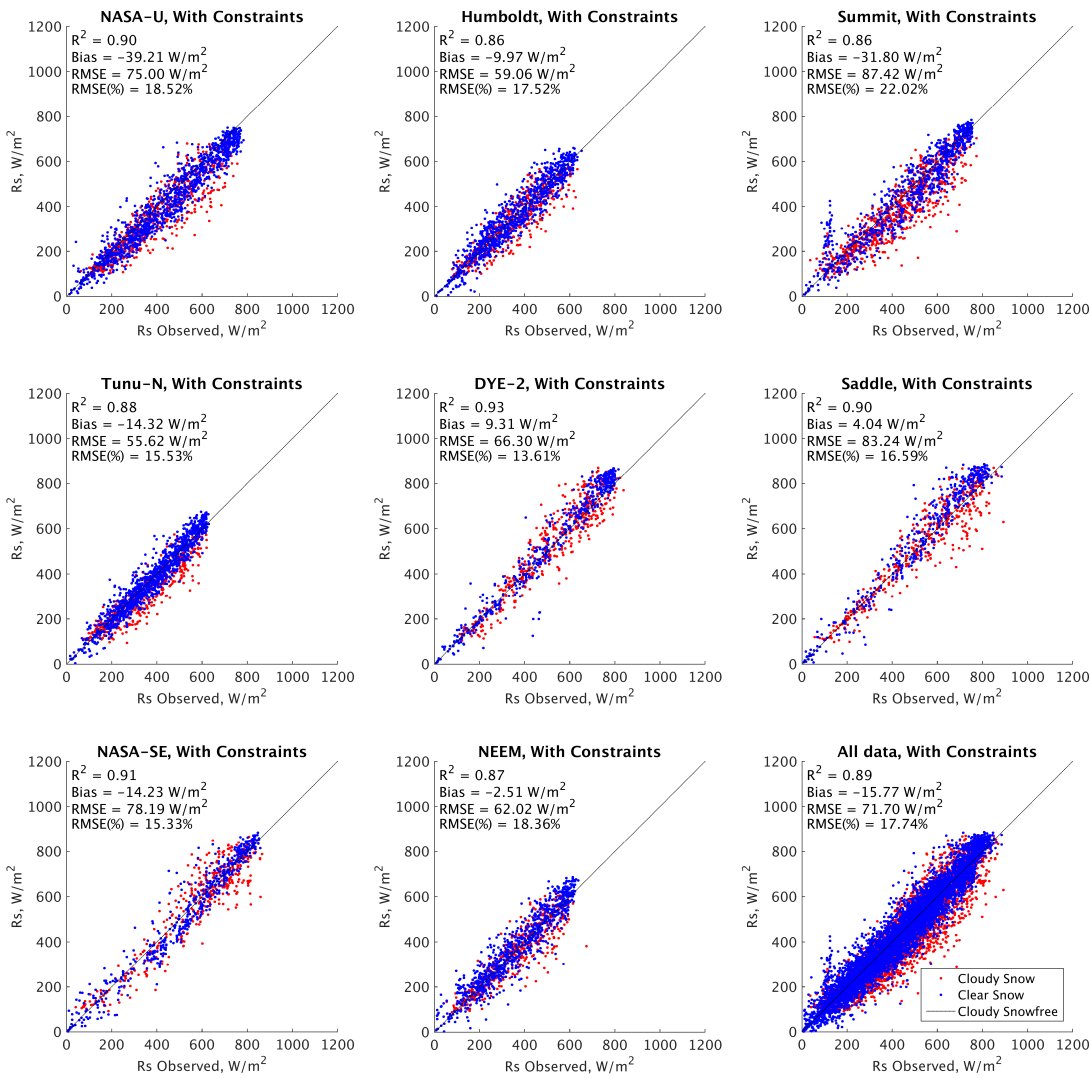

Figure 6 Scatterplot of instantaneous ISR in 2013 at GC-Net sites. (Blue: clear-sky results Red: cloudy-sky results)

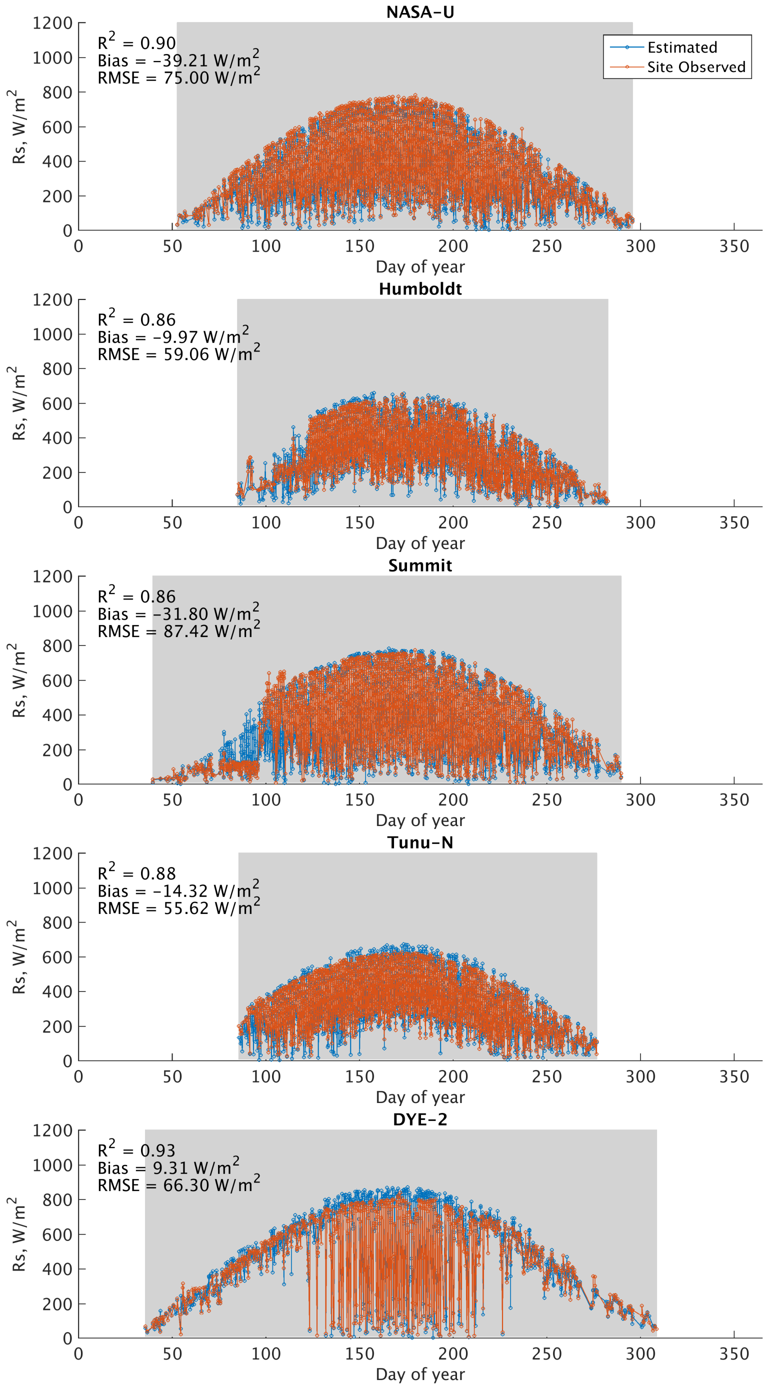

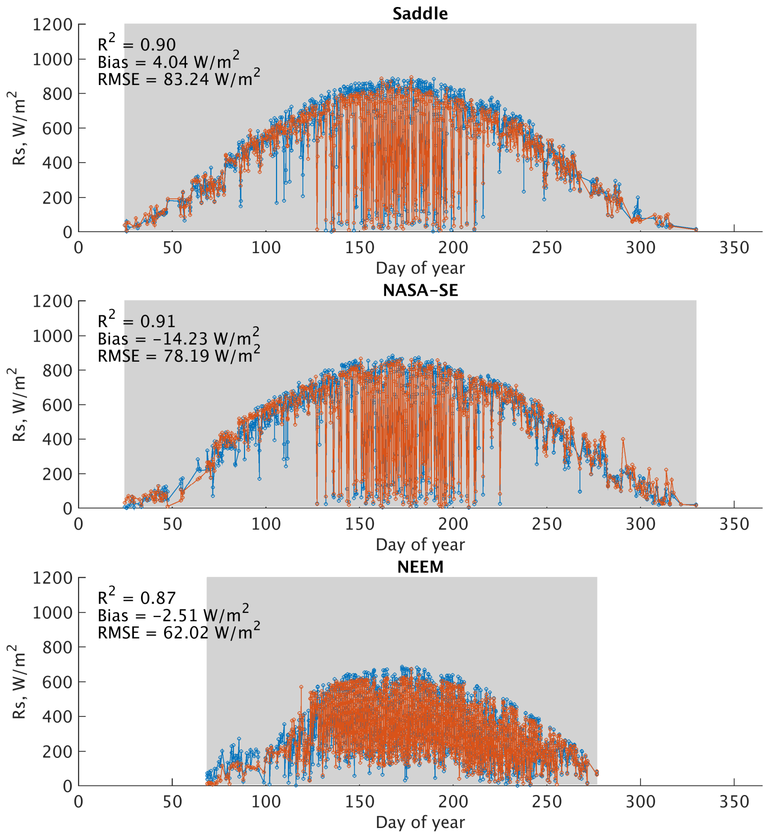

Figure 7 Validation of time series for instantaneous ISR in 2013 at GC-Net sites. (Blue: estimated results, Red: GC-Net site observation data, the gray area denotes observation over snow, missing data are due to data gap from field observations)

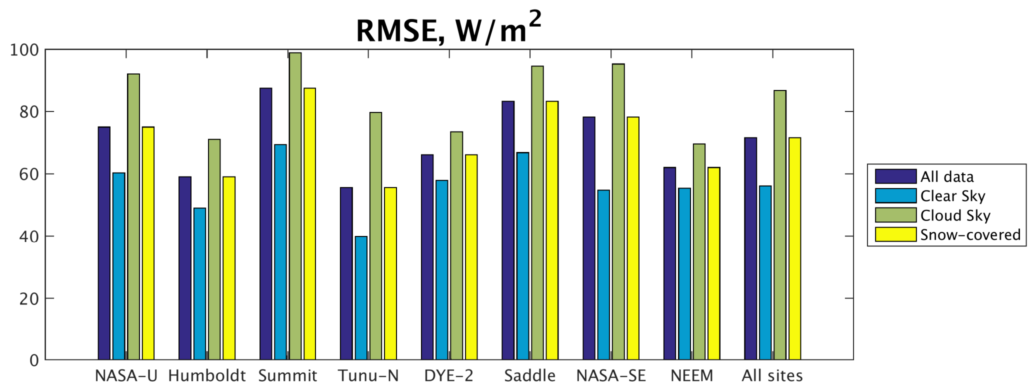

Figure 8 Validation RMSE for clear/cloudy/all sky and over snow cases at GC-Net sites

The results from the GC-Net sites had larger bias errors and RMSEs compared with those of the SURFRAD sites; this is clearer in the relative RMSE than in the absolute value. Snow-covered surfaces bring uncertainties to the estimation, especially in cloudy-sky cases. On the other hand, we obtained more satellite observations in the Arctic region, which provided enough information for the optimization. The GC-Net validation results show that the proposed algorithm was capable of estimating ISR for permanent-snow cases.

4.3 Analysis of impacts from constraints and cloud-screening analysis of impacts

In the estimation algorithm, we used several optional products as optional constraints; these include MODIS surface albedo (MCD43), MODIS AOD (MOD/MYD04), and MODIS COD (MOD/MYD06). In the validation procedure, we introduced a cloud-screening process (the cloud screening process was discussed in Section 2.3). The validation results for different estimation and validation strategies are shown in Figures 9 and 10 and Tables 2–7. The inclusive of constraints led to a decrease of approximately 5 and 13 W/m^2 in RMSEs at the SURFRAD and GC-Net sites, respectively; the cloud-screening process lowered the RMSE by about 17 W/m^2 at the SURFRAD sites. The reduced RMSE at each site from the constraints and the cloud screening are shown in Figures 11 and 12. At the SURFRAD sites, the largest RMSE decrease from constraints was found at the Penn State site. At the Fort Peck site, the inclusive of constraints increased the RMSE, which meant that the uncertainties from the optional constraints sometimes lowered the accuracy. The largest difference after the cloud-screening process was found at the Boulder site, as this site is located in the Table Mountain and is more often affected by sparse cloud cover. At the GC-Net sites, decreases in RMSEs were generally less than those at the SURFRAD sites. This is because more observations were acquired in the Arctic region and used in the optimization; therefore the TOA reflectance contributed relatively more information compared with that in lower latitudes.

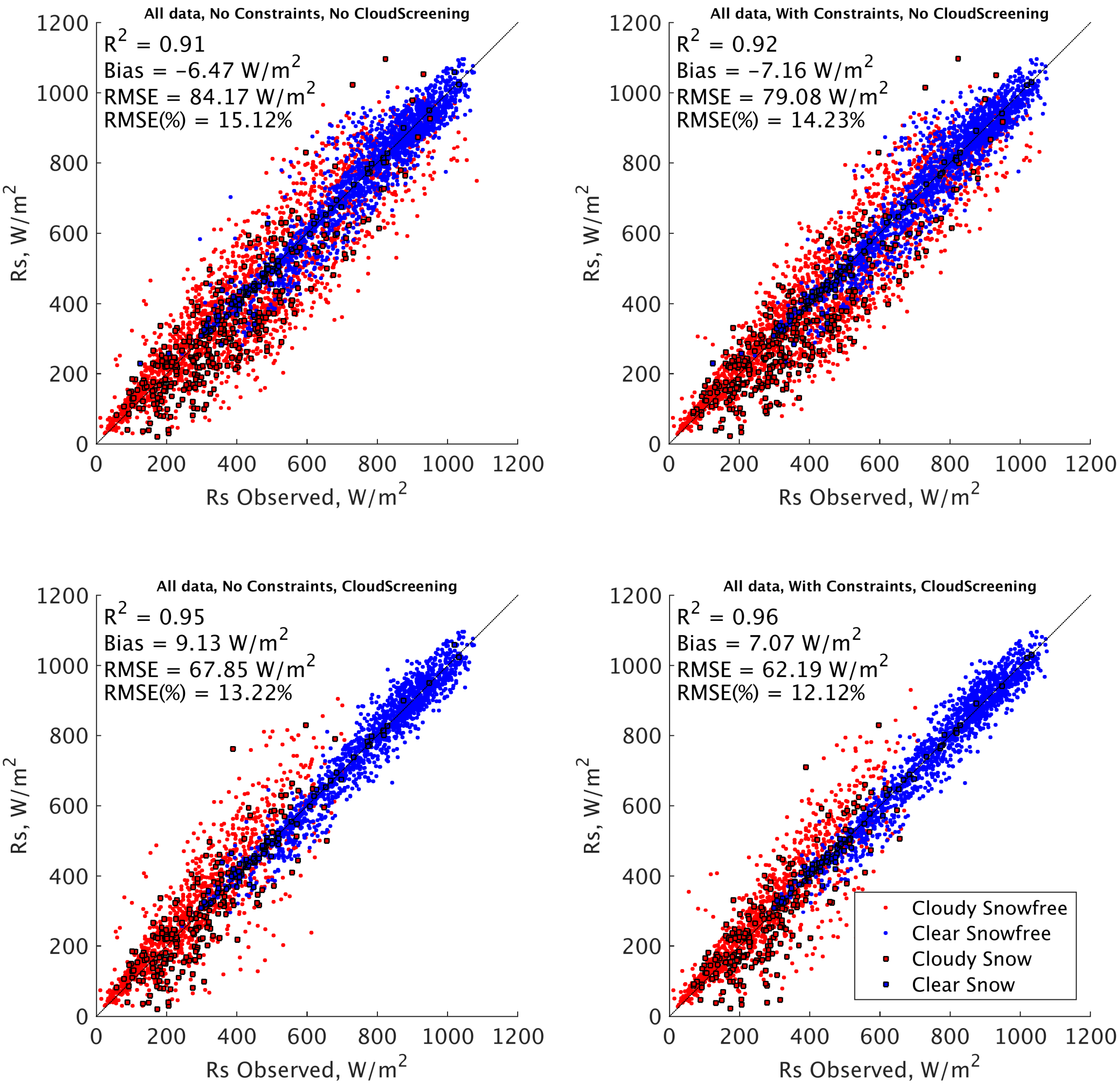

Figure 9 Impact of constraints and cloud-screening on the estimated and site observed ISR at SURFRAD sites

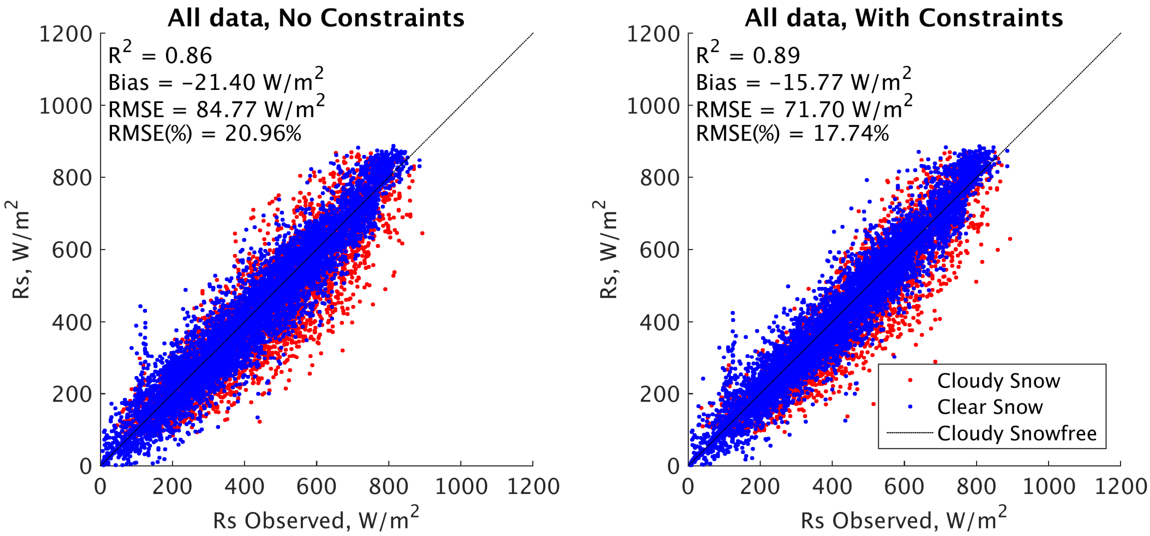

Figure 10 Impact of constraints and cloud-screening on the estimated and site observed ISR at GC-Net sites

Table 2 Validation results at SURFRAD site without constraints and cloud-screening

Sites	R^2	Bias, W/ m^2	RMSE, W/ m^2	RMSE, %	Clear RMSE	Cloudy RMSE	Snow RMSE
Fort Peck	0.92	-2.23	73.27	14.26	49.62	84.69	73.46
Sioux Falls	0.91	-7.39	80.73	15.92	48.05	95.37	89.41
Penn State	0.92	6.05	83.51	17.59	63.99	89.33	76.30
Bondville	0.91	-7.96	84.95	16.58	59.92	96.08	90.71
Boulder	0.85	-25.94	109.12	18.17	67.13	134.39	120.23
Desert Rock	0.92	-14.86	68.51	9.32	52.17	100.04	NAN
Goodwin Creek	0.92	8.22	83.13	14.79	70.41	91.46	NAN
All	0.91	-6.47	84.17	15.12	58.50	98.96	86.58

Table 3 Validation results at SURFRAD site with constraints

Sites	R^2	Bias, W/ m^2	RMSE, W/ m^2	RMSE, %	Clear RMSE	Cloudy RMSE	Snow RMSE
Fort Peck	0.93	-4.14	71.94	13.97	47.57	83.51	75.76
Sioux Falls	0.91	-9.32	82.08	16.15	49.87	96.45	89.66
Penn State	0.93	6.35	76.30	16.11	62.70	80.50	71.59
Bondville	0.92	-8.74	77.18	15.01	56.46	86.70	82.31
Boulder	0.87	-23.35	99.10	16.57	63.10	121.25	120.45
Desert Rock	0.93	-15.87	67.33	9.16	51.48	97.74	NAN
Goodwin Creek	0.93	5.90	75.47	13.59	66.85	81.24	NAN
All	0.92	-7.16	79.08	14.23	56.51	92.26	86.23

Table 4 Validation results at SURFRAD site with cloud-screening

Sites	R^2	Bias, W/ m^2	RMSE, W/ m^2	RMSE, %	Clear RMSE	Cloudy RMSE	Snow RMSE

Fort Peck	0.96	15.44	57.08	12.18	37.23	69.79	55.95
Sioux Falls	0.94	10.38	67.25	14.39	43.07	81.50	75.65
Penn State	0.95	24.00	69.86	18.01	45.04	77.46	54.37
Bondville	0.94	6.55	68.87	15.36	39.68	83.58	94.13
Boulder	0.92	-2.39	80.66	14.05	46.16	111.21	103.56
Desert Rock	0.94	0.38	56.90	7.58	43.97	109.61	NAN
Goodwin Creek	0.94	8.85	73.54	14.90	46.99	92.50	NAN
All	0.95	9.13	67.85	13.22	43.31	86.01	71.03

Table 5 Validation results at SURFRAD site with constraints and cloud-screening

Sites	**R^2**	**Bias, W/ m^2**	**RMSE, W/ m^2**	**RMSE, %**	**Clear RMSE**	**Cloudy RMSE**	**Snow RMSE**
Fort Peck	0.96	13.18	56.71	12.01	38.26	68.80	60.64
Sioux Falls	0.94	8.94	67.65	14.43	41.94	82.46	80.11
Penn State	0.96	20.11	59.48	15.37	42.41	64.97	50.56
Bondville	0.95	3.48	63.08	14.06	35.85	76.79	83.80
Boulder	0.94	-2.34	73.58	12.85	43.74	100.48	95.46
Desert Rock	0.95	-1.78	51.75	6.89	43.32	89.86	NAN
Goodwin Creek	0.96	7.44	61.37	12.54	45.07	73.69	NAN
All	0.96	7.07	62.19	12.12	41.85	77.65	71.75

Table 6 Validation results at GC-Net site without constraints

Sites	**R^2**	**Bias, W/ m^2**	**RMSE, W/ m^2**	**RMSE, %**	**Clear RMSE**	**Cloudy RMSE**
NASA-U	0.86	-46.48	88.62	21.85	65.44	113.48
Humboldt	0.81	-12.64	69.22	20.55	56.62	84.52
Summit	0.84	-39.39	96.48	24.29	76.88	108.89
Tunu-N	0.81	-21.56	73.59	20.53	46.17	111.80
DYE-2	0.88	6.72	88.26	18.05	58.20	108.23
Saddle	0.88	3.85	88.41	17.59	68.39	101.73
NASA-SE	0.88	-22.68	93.82	18.43	56.17	119.23
NEEM	0.80	-8.26	77.42	22.92	64.43	91.75
All	0.86	-21.40	84.77	20.96	61.65	105.77

Table 7 Validation results at GC-Net site with constraints

Sites	**R^2**	**Bias, W/m^2**	**RMSE, W/ m^2**	**RMSE, %**	**Clear RMSE**	**Cloudy RMSE**
NASA-U	0.90	-39.21	75.00	18.52	60.28	92.12
Humboldt	0.86	-9.97	59.06	17.52	49.01	71.14
Summit	0.86	-31.80	87.42	22.02	69.47	98.89
Tunu-N	0.88	-14.32	55.62	15.53	39.90	79.69
DYE-2	0.93	9.31	66.30	13.61	57.90	73.51
Saddle	0.90	4.04	83.24	16.59	66.95	94.60

NASA-SE	0.91	-14.23	78.19	15.33	54.73	95.30
NEEM	0.87	-2.51	62.02	18.36	55.41	69.75
All	0.89	-15.77	71.70	17.74	56.14	86.69

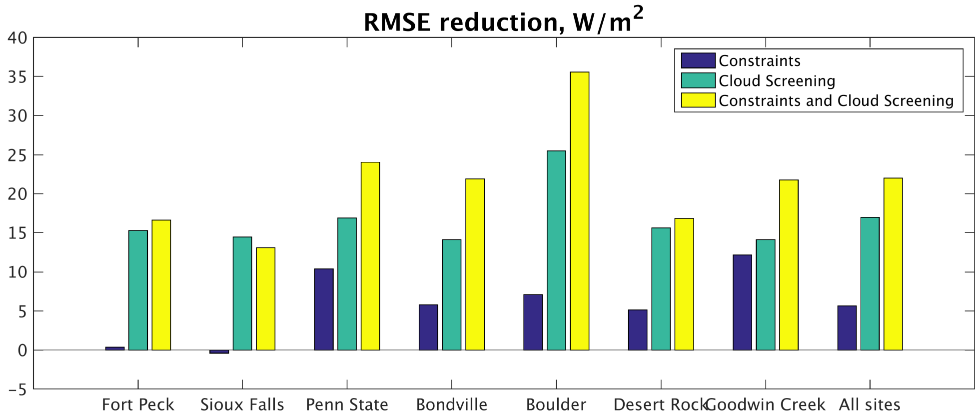

Figure 11 Impact of constraints and cloud-screening on the validation RMSE at SURFRAD sites

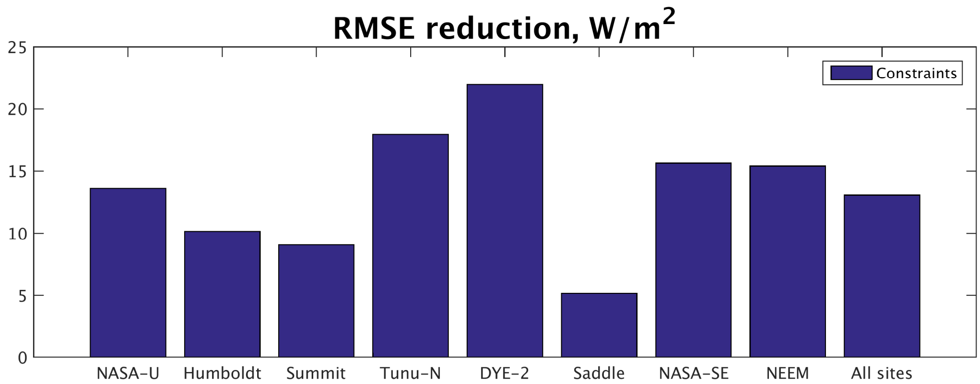

Figure 12 Impact of constraints and on the validation RMSE at GC-Net sites

5. **Conclusions**

The goal of this study was to estimate high-resolution surface ISR from MODIS TOA observations. We assumed that the surface BRDF parameters remained stable within a short time window. Subsequently, we simulated atmospheric transmittance in each atmospheric condition (AOD/COD). With the modeled BRDF parameters and simulated atmospheric transmittance, we calculated TOA reflectance and then optimized the BRDF parameters and atmospheric conditions (AOD/COD). Finally, we estimated ISR based on the surface BRDF parameters and atmospheric conditions. We validated the estimated ISR using ground data measured in 2013 at seven SURFRAD and 8 GC-Net sites. The validation results showed sufficient accuracy at both snow-free and snow-covered sites. The SURFRAD site validation showed an R^2 of 0.91, a bias of -6.47 W/m^2, and an RMSE of 84.17 W/m^2 (15.12%); the GC-Net validation showed an R^2 of 0.86, a bias of -21.40 W/m^2, and an RMSE of 84.77 W/m^2 (20.96%) for instantaneous ISR.

The algorithm has several advantages: First, most of other methods rely on input data. However, many input data, especially the atmospheric data (e.g. AOD, COD) have large uncertainties. The uncertainties from input data accumulated in the estimation algorithms and cause larger influence on the results. The proposed method relies on multispectral satellite observations and can distinguish the information from the atmosphere and the surface directly from the TOA information. High-level products (surface and atmospheric) are not required input but serve as optional constraints. This helps improve the estimates of surface incident radiation.

Secondly, this algorithm could estimate ISR with a higher accuracy than existing products and algorithms could at the SURFRAD and GC-NET sites. The validation at the SURFRAD and GC-Net sites showed a bias of 7.07 and -15.77 W/m^2, and an RMSE of 62.19 W/m^2 (12.12%) and 71.70 W/m^2 (17.74%), respectively. Many previous studies assessed the widely used satellite-based products and revealed larger uncertainties. (Gui et al. 2010; Jia et al. 2013; Zhang et al. 2013; Zhang et al. 2014), showing an RMSE of 80~150 W/m^2 for hourly/3-hourly ISR at the same SURFRAD sites. Most existing methods calculate ISR based on surface and atmospheric products. The uncertainties from each of the products may be accumulated to produce a much larger error in the estimated ISR. In the proposed method, however, the products could be used as constraints in the cost function to aid the optimization, but they were optional inputs. The proposed algorithm mainly relied on multiple TOA observations from sensors and is a direct retrieval method. Second, this algorithm could estimate other surface parameters, including surface band reflectance and surface broadband albedo. Third, this algorithm could estimate ISR under different atmospheric and surface conditions, including clear-sky and cloudy-sky conditions as well as snow-free and snow-covered surfaces.

Furthermore, we analyzed the improvement of accuracy using MODIS AOD, COD, and surface albedo data as cost function constraints. When the AOD and COD estimates were constrained, validation results indicated RMSE reductions of 21.98 W/m^2 and 13.07 W/m^2 at the SURFRAD and GC-Net sites, respectively. Additional products may help the optimization but may also bring uncertainties. In the snow-free cases, the improvement was significant at most sites. However, in the snow-covered cases, the RMSE decrease was smaller. The combination of greater information and uncertainty resulted in a smaller improvement in the Arctic region than in lower latitude. This was due to more observations from TOA at high latitudes and more uncertainties in the MODIS atmospheric products in these regions.

However, the proposed algorithm had some limitations. The algorithm relied on cloud mask data to distinguish clear-sky and cloudy-sky conditions, but the cloud mask data may be unreliable in snow-covered areas, which may limit the accuracy of ISR estimation. Furthermore, the optimization process was relatively time-consuming. Further efforts will be made to improve the efficiency in mainly two ways: 1) improving the efficiency of the optimization method by using more a rapid convergence approach, and 2) replacing the LUT with parameterization.

Acknowledgements

This research was supported by the National Aeronautics and Space Administration (NASA) under grant NNH13ZDA001N-TERAQ and NOAA JPSS funding through the University of Maryland and National Natural Science Foundation of China grant 41771379. We gratefully acknowledge the MODIS team for providing access to the land and atmosphere products online. We also thank the SURFRAD, GC-Net teams for providing and maintaining all the data sets used for the validation in this study. We would also like to thank the editor and the anonymous reviewers for their helpful suggestions

References

Aguiar, L.M., Pereira, B., David, M., Diaz, F., & Lauret, P. (2015). Use Of Satellite Data To Improve Solar Radiation Forecasting With Bayesian Artificial Neural Networks. *Solar Energy, 122*, 1309-1324

Akarslan, E., & Hocaoglu, F.O. (2016). A Novel Adaptive Approach For Hourly Solar Radiation Forecasting. *Renewable Energy, 87*, 628-633

Akarslan, E., Hocaoglu, F.O., & Edizkan, R. (2014). A Novel M-D (Multi-Dimensional) Linear Prediction Filter Approach For Hourly Solar Radiation Forecasting. *Energy, 73*, 978-986

Augustine, J.A., Deluisi, J.J., & Long, C.N. (2000). Surfrad - A National Surface Radiation Budget Network For Atmospheric Research. *Bulletin Of The American Meteorological Society, 81*, 2341-2357

Baldocchi, D., Falge, E., Gu, L.H., Olson, R., Hollinger, D., Running, S., Anthoni, P., Bernhofer, C., Davis, K., Evans, R., Fuentes, J., Goldstein, A., Katul, G., Law, B., Lee, X.H., Malhi, Y., Meyers, T., Munger, W., Oechel, W., U, K.T.P., Pilegaard, K., Schmid, H.P., Valentini, R., Verma, S., Vesala, T., Wilson, K., & Wofsy, S. (2001). Fluxnet: A New Tool To Study The Temporal And Spatial Variability Of Ecosystem-Scale Carbon Dioxide, Water Vapor, And Energy Flux Densities. *Bulletin Of The American Meteorological Society, 82*, 2415-2434

Bisht, G., & Bras, R.L. (2010). Estimation Of Net Radiation From The Modis Data Under All Sky Conditions: Southern Great Plains Case Study. *Remote Sensing Of Environment, 114*, 1522-1534

Breon, F.M., Maignan, F., Leroy, M., & Grant, I. (2002). Analysis Of Hot Spot Directional Signatures Measured From Space. *Journal Of Geophysical Research-Atmospheres, 107*

Duan, Q.Y., Sorooshian, S., & Gupta, V.K. (1994). Optimal Use Of The Sce-Ua Global Optimization Method For Calibrating Watershed Models. *Journal Of Hydrology, 158*, 265-284

Forman, B.A., & Margulis, S.A. (2009). High-Resolution Satellite-Based Cloud-Coupled Estimates Of Total Downwelling Surface Radiation For Hydrologic Modelling Applications. *Hydrology And Earth System Sciences, 13*, 969-986

Gilgen, H., & Ohmura, A. (1999). The Global Energy Balance Archive. *Bulletin Of The American Meteorological Society, 80*, 831-850

Gui, S., Liang, S., Wang, K., Li, L., & Zhang, X. (2010). Assessment Of Three Satellite-Estimated Land Surface Downwelling Shortwave Irradiance Data Sets. *Ieee Geoscience And Remote Sensing Letters, 7*, 776-780

He, T., Liang, S., Wang, D., Wu, H., Yu, Y., & Wang, J. (2012). Estimation Of Surface Albedo And Directional Reflectance From Moderate Resolution Imaging Spectroradiometer (Modis) Observations. *Remote Sensing Of Environment, 119*, 286-300

Huang, G.H., Li, X., Huang, C.L., Liu, S.M., Ma, Y.F., & Chen, H. (2016a). Representativeness Errors Of Point-Scale Ground-Based Solar Radiation Measurements In The Validation Of Remote Sensing Products. *Remote Sensing Of Environment, 181*, 198-206

Huang, G.H., Li, X., Ma, M.G., Li, H.Y., & Huang, C.L. (2016b). High Resolution Surface Radiation Products For Studies Of Regional Energy, Hydrologic And Ecological Processes Over Heihe River Basin, Northwest China. *Agricultural And Forest Meteorology, 230*, 67-78

Huang, G.H., Ma, M.G., Liang, S.L., Liu, S.M., & Li, X. (2011). A Lut-Based Approach To Estimate Surface Solar Irradiance By Combining Modis And Mtsat Data. *Journal Of Geophysical Research-Atmospheres, 116*

Janjai, S., Pankaew, P., & Laksanaboonsong, J. (2009). A Model For Calculating Hourly Global Solar Radiation From Satellite Data In The Tropics. *Applied Energy, 86*, 1450-1457

Jia, B., Xie, Z., Dai, A., Shi, C., & Chen, F. (2013). Evaluation Of Satellite And Reanalysis Products Of Downward Surface Solar Radiation Over East Asia: Spatial And Seasonal Variations. *Journal Of Geophysical Research-Atmospheres, 118*, 3431-3446

Levy, R.C., Remer, L.A., Kleidman, R.G., Mattoo, S., Ichoku, C., Kahn, R., & Eck, T.F. (2010). Global Evaluation Of The Collection 5 Modis Dark-Target Aerosol Products Over Land. *Atmospheric Chemistry And Physics, 10*, 10399-10420

Liang, S., Wang, K., Zhang, X., & Wild, M. (2010). Review On Estimation Of Land Surface Radiation And Energy Budgets From Ground Measurement, Remote Sensing And Model Simulations. *Ieee Journal Of Selected Topics In Applied Earth Observations And Remote Sensing, 3*, 225-240

Liang, S., Zheng, T., Liu, R., Fang, H., Tsay, S.-C., & Running, S. (2006). Estimation Of Incident Photosynthetically Active Radiation From Moderate Resolution Imaging Spectrometer Data. *Journal Of Geophysical Research-Atmospheres, 111*

Liang, S.L., & Strahler, A.H. (1994). 4-Stream Solution For Atmospheric Radiative-Transfer Over A Non-Lambertian Surface. *Applied Optics, 33*, 5745-5753

Liang, S.L., & Strahler, A.H. (1995). An Analytic Radiative-Transfer Model For A Coupled Atmosphere And Leaf Canopy. *Journal Of Geophysical Research-Atmospheres, 100*, 5085-5094

Maignan, F., Breon, F.M., & Lacaze, R. (2004). Bidirectional Reflectance Of Earth Targets: Evaluation Of Analytical Models Using A Large Set Of Spaceborne Measurements With Emphasis On The Hot Spot. *Remote Sensing Of Environment, 90*, 210-220

Mayer, B., & Kylling, A. (2005). Technical Note: The Libradtran Software Package For Radiative Transfer Calculations - Description And Examples Of Use. *Atmospheric Chemistry And Physics, 5*, 1855-1877

Meador, W.E., & Weaver, W.R. (1980). 2-Stream Approximations To Radiative-Transfer In Planetary-Atmospheres - A Unified Description Of Existing Methods And A New Improvement. *Journal Of The Atmospheric Sciences, 37*, 630-643

Mefti, A., Adane, A., & Bouroubi, M.Y. (2008). Satellite Approach Based On Cloud Cover Classification: Estimation Of Hourly Global Solar Radiation From Meteosat Images. *Energy Conversion And Management, 49*, 652-659

Ohmura, A., Dutton, E.G., Forgan, B., Frohlich, C., Gilgen, H., Hegner, H., Heimo, A., Konig-Langlo, G., Mcarthur, B., Muller, G., Philipona, R., Pinker, R., Whitlock, C.H., Dehne, K., & Wild, M. (1998). Baseline Surface Radiation Network (Bsrn/Wcrp): New Precision Radiometry For Climate Research. *Bulletin Of The American Meteorological Society, 79*, 2115-2136

Pokrovsky, O., & Roujean, J.L. (2003a). Land Surface Albedo Retrieval Via Kernel-Based Brdf Modeling: I. Statistical Inversion Method And Model Comparison. *Remote Sensing Of Environment, 84*, 100-119

Pokrovsky, O., & Roujean, J.L. (2003b). Land Surface Albedo Retrieval Via Kernel-Based Brdf Modeling: Ii. An Optimal Design Scheme For The Angular Sampling. *Remote Sensing Of Environment, 84*, 120-142

Qin, J., Tang, W., Yang, K., Lu, N., Niu, X., & Liang, S. (2015). An Efficient Physically Based Parameterization To Derive Surface Solar Irradiance Based On Satellite Atmospheric Products. *Journal Of Geophysical Research-Atmospheres, 120*, 4975-4988

Qin, W.H., Herman, J.R., & Ahmad, Z. (2001). A Fast, Accurate Algorithm To Account For Non-Lambertian Surface Effects On Toa Radiance. *Journal Of Geophysical Research-Atmospheres, 106*, 22671-22684

Steffen, K., Box, J., & Abdalati, W. (1996). Greenland Climate Network: Gc-Net. *Us Army Cold Regions Reattach And Engineering (Crrel), Crrel Special Report*, 98-103

Tang, W.J., Qin, J., Yang, K., Liu, S.M., Lu, N., & Niu, X.L. (2016). Retrieving High-Resolution Surface Solar Radiation With Cloud Parameters Derived By Combining Modis And Mtsat Data. *Atmospheric Chemistry And Physics, 16*, 2543-2557

Van Laake, P.E., & Sanchez-Azofeifa, G.A. (2004). Simplified Atmospheric Radiative Transfer Modelling For Estimating Incident Par Using Modis Atmosphere Products. *Remote Sensing Of Environment, 91*, 98-113

Wild, M., Folini, D., Schar, C., Loeb, N., Dutton, E.G., & Konig-Langlo, G. (2013). The Global Energy Balance From A Surface Perspective. *Climate Dynamics, 40*, 3107-3134

Zhang, T., Stackhouse, P.W., Jr., Gupta, S.K., Cox, S.J., Mikovitz, J.C., & Hinkelman, L.M. (2013). The Validation Of The Gewex Srb Surface Shortwave Flux Data Products Using Bsrn Measurements: A Systematic Quality Control, Production And Application Approach. *Journal Of Quantitative Spectroscopy & Radiative Transfer, 122*, 127-140

Zhang, X., Liang, S., Wild, M., & Jiang, B. (2015). Analysis Of Surface Incident Shortwave Radiation From Four Satellite Products. *Remote Sensing Of Environment, 165*, 186-202

Zhang, X., Liang, S., Zhou, G., Wu, H., & Zhao, X. (2014). Generating Global Land Surface Satellite Incident Shortwave Radiation And Photosynthetically Active Radiation Products From Multiple Satellite Data. *Remote Sensing Of Environment, 152*, 318-332

Zhang, X.T., Liang, S.L., Wang, G.X., Yao, Y.J., Jiang, B., & Cheng, J. (2016). Evaluation Of The Reanalysis Surface Incident Shortwave Radiation Products From Ncep, Ecmwf, Gsfc, And Jma Using Satellite And Surface Observations. *Remote Sensing, 8*, 24

LIST OF FIGURE CAPTIONS